Entropic Comparison of Atomic-Resolution Electron Tomography of Crystals and Amorphous Materials

S. M. Collins,[1] R. K. Leary,[1] P. A. Midgley,[1] R. Tovey,[2] M. Benning,[2] C.-B. Schönlieb,[2] P. Rez,[3] and M. M. J. Treacy[3,1,*]
[1]*Department of Materials Science and Metallurgy, University of Cambridge,*
27 Charles Babbage Road, Cambridge CB3 0FS, United Kingdom
[2]*DAMTP, Centre for Mathematical Sciences, University of Cambridge, Wilberforce Road, Cambridge CB3 0WA, United Kingdom*
[3]*Department of Physics, Arizona State University, Tempe, Arizona 85287, USA*

(Received 26 April 2017; published 16 October 2017)

Electron tomography bears promise for widespread determination of the three-dimensional arrangement of atoms in solids. However, it remains unclear whether methods successful for crystals are optimal for amorphous solids. Here, we explore the relative difficulty encountered in atomic-resolution tomography of crystalline and amorphous nanoparticles. We define an informational entropy to reveal the inherent importance of low-entropy zone-axis projections in the reconstruction of crystals. In turn, we propose considerations for optimal sampling for tomography of ordered and disordered materials.

DOI: 10.1103/PhysRevLett.119.166101

Electron tomography has now advanced to the point where up to 100 000 atoms in small crystalline particles can be located with plausible accuracy [1–9]. Although there are still details to resolve, this is an important advance for materials science, particularly for the study of crystalline particle surfaces, internal defects, and associated strain fields [4,5,8]. Electron tomography of proteins and virus particles has also advanced impressively, and it is already a mainstream tool with well-established protocols [10–12]. The biological work does not quite achieve true atomic resolution but instead infers structure from near-atomic-resolution data and knowledge of the component molecular groups.

These recent successes with crystals have led to the conjecture that the atomic structures of amorphous materials could now be resolved in three dimensions [5,13]. If possible, this would represent a major breakthrough. The structures of amorphous materials are known only at a statistical level, such as in the form of the radial density function (RDF) obtained by high-resolution diffraction. RDFs are effective for revealing short-range order, but they are less sensitive to medium-range order at 0.5–3 nm length scales. Fluctuation electron microscopy can reveal the presence and type of medium-range order, but again only as a statistical measure [14,15]. Although tomographic reconstructions of crystals do not appear to rely explicitly on their crystalline regularity [5], intuitively their periodic degeneracy should render them easier to solve than disordered materials. In this Letter, we quantify the relative difficulty of performing electron tomography on models of crystals and glasses using an entropic approach.

Two 5.0 nm diameter spheroidal models of silicon were generated. The first had a cubic-diamond crystalline silicon structure. The second was extracted from a 100 000-atom amorphous-Si model made by Barkema and Mousseau [16], with the density decreased by 4.67% to match that of the crystalline structure. Both models were trimmed to 3409 atoms. The models were tetrahedrally coordinated in the interior, with a mean bond distance of ∼0.235 nm. To gain insight into the essential physics underpinning atomic-resolution electron tomography, a simplified model is presented here first, and then the findings are subsequently applied to realistic electron tomographic reconstructions in order to verify the predictions of the model.

Projections were first simulated by treating atoms as idealized points while assuming perfect imaging conditions. Image intensity was proportional to the projected mass thickness of the spheres intersecting each pixel. The side length of voxels and pixels in projection images were identical and fixed at 0.0405 nm. For these pointlike atomic models, images were assigned 10^6 electron counts (entire image), emulating typical shot noise. Models were rotated about one axis, and projections perpendicular to that axis were examined. For the crystalline model, two rotation axes were investigated, the cubic [001] and [101] axes, as they presented a series of different zone axes. For the amorphous model, a single rotation axis was used, as all axes are statistically equivalent. We assume that images are recorded with 100% detection quantum efficiency.

To estimate the relative information, the two-dimensional (2D) $(N \times N)$-pixel image $I^{(2)}_{jk}$ is treated as a projection along i of a three-dimensional (3D) $(N \times N \times N)$-voxel object, with values $I^{(3)}_{ijk}$. Ideally, the goal of tomography is to solve the $I^{(3)}_{ijk}$ values unambiguously. Each pixel in an image is the accumulation of intensities along a column of N voxels. Thus, $I^{(2)}_{jk} = \sum_{i=1}^{N} I^{(3)}_{ijk}$. A single projection generally has insufficient information to solve $I^{(3)}_{ijk}$. We wish to estimate that ambiguity. Under the positivity constraint, $I^{(3)}_{ijk} \geq 0; I^{(2)}_{jk} \geq 0$, and using the "stars and bars" method [17], the number of ways integer intensity can be distributed among N voxels is $W_{jk} = (I_{jk}^{(2)} + N - 1)!/I_{jk}^{(2)}!(N-1)!$. Treating adjacent pixels as independent, the total number of arrangements for the image is $W = \prod_{j=1}^{N} \prod_{k=1}^{N} W_{jk}$.

An informational entropy, $S = \ln(W)$, can be defined and interpreted as being a measure of the ambiguity of the 3D intensity distribution as constrained by the projection. $S = 0$, i.e., $W = 1$, corresponds to a unique solution. Using Stirling's approximation, we obtain

$$S \approx \sum_{j=1}^{N} \sum_{k=1}^{N} \left[I_{jk}^{(2)} \ln\left(\frac{I_{jk}^{(2)} + N - 1}{I_{jk}^{(2)}} \right) + (N-1) \ln\left(\frac{I_{jk}^{(2)} + N - 1}{N - 1} \right) \right], \qquad (1)$$

which is also appropriate for noninteger intensities. If intensities are not integers, the gamma function form can be used for W_{jk}: $W_{jk} = \Gamma(I_{jk}^{(2)} + N)/\Gamma(I_{jk}^{(2)} + 1)(N-1)!$. Pixels with $I_{jk}^{(2)} = 0$ contribute zero to S since column jk is solved unambiguously under the positivity constraint. This definition of the entropy S does not specify or make assumptions about the atomicity of the object considered for tilt-series tomography. As such, no restrictions on the atom locations within the volume have been imposed on the calculation of entropy. Rather, S is given in terms of the image intensities, which can be arranged freely throughout the volume.

Figure 1(a) (left side) plots the entropic density, S/N^3 per voxel, as a function of the projection angle of the models. The amorphous model (the solid line) has an approximately constant trace, whereas the crystalline models (the dashed lines) exhibit strong dips at the zone axes. Views of the models at selected angles are inserted in the figure.

Zone-axis views present atoms lined up in columns, minimizing their projected area and exposing the intercolumn gaps, increasing the number of pixels with zero intensity. Since no voxel can have negative intensity, all N voxels along that projection must also have zero intensity and are solved immediately. Zone-axis views strongly constrain the solution because they efficiently tell us where the sparsely populated voxels lie. Amorphous structures do not have such efficiently eclipsed projections, so they generally have higher entropy. In Fig. 1(a) the amorphous entropy (the solid line on the left side) is always higher than the crystal entropy (the dashed lines). Some off-zone-axis crystal views, such as those for the tilts about [001], can have entropy comparable to that for the amorphous solid. The views for tilts about [101] systematically have lower entropy than the amorphous particle because the (101) planes (and the gaps between them), with a spacing of 0.384 nm, are prominently visible throughout the tilt series. Real data do not have many zero-intensity pixels, so entropy provides a better metric than a simple count of the zero-intensity pixels. For the consistent set analyzed here, the crystalline zone-axis views are inherently more informative (i.e., have a lower S) than the non-zone-axis viewing directions or the amorphous views.

Tomography uses multiple views of the object in order to reduce the ambiguity in the 3D intensity distribution. Each projection adds information, so both W and S should decrease as the constraints provided by additional image projections are applied. In principle, we seek to minimize

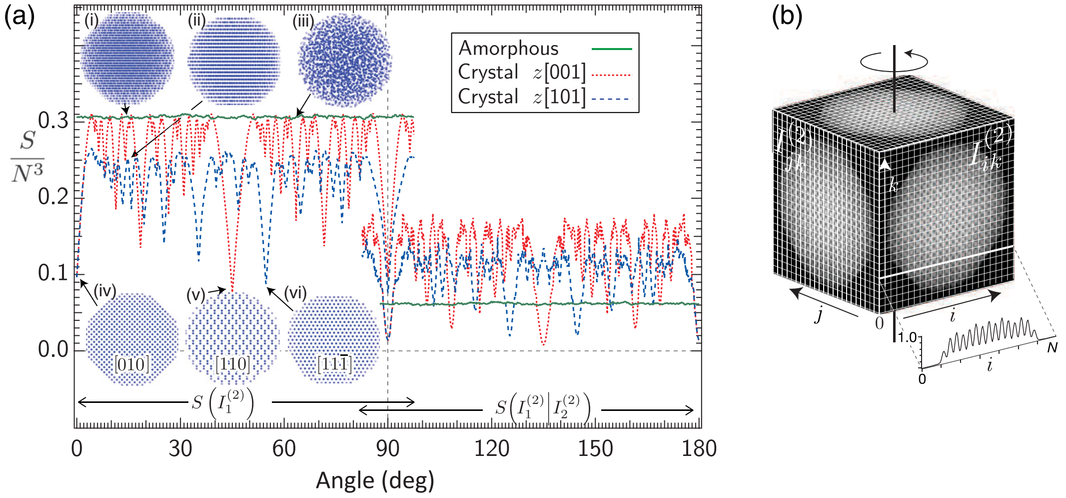

FIG. 1. (a) Normalized informational entropy for three models plotted as a function of particle rotation (about the vertical axis). Plots are mirror symmetric about the 90° abscissa, and just over half of the range of each plot is shown. (Left side) Projection entropies, $S(I_1^{(2)})$. (Right side) Joint entropies $S(I_1^{(2)}|I_2^{(2)})$. Five views of the crystalline model and one view of the amorphous model are shown. (i),(ii) Crystals rotated 13.6° from the [010] projection about the [001] and [101] axes, respectively. (iii) Random amorphous view. (iv),(v),(vi) Crystals viewed down the [010], [110], and [11$\bar{1}$] zone axes, respectively. (b) Representation of the 3D voxel volume, showing three perpendicular projections of a particle. The intensity trace along i in the view $I_{ik}^{(2)}$ is normalized to its maximum value.

$S(I^{(3)}|\{I_n^{(2)}\})$, where $I^{(3)}$ is the full 3D voxel space solution, and $\{I_n^{(2)}\}$ is the constraining set of 2D projections. An entropic approach to tomography involves the application of combinatorial constraints, which does not appear to be a solved problem for arbitrary projections [18–23]. Here, we apply an ansatz that will allow us to estimate the combinatorial constraints provided by two perpendicular views.

For two perpendicular image projections, $I_{jk}^{(2)} = \sum_{i=1}^{N} I_{ijk}^{(3)}$ and $I_{ik}^{(2)} = \sum_{j=1}^{N} I_{ijk}^{(3)}$ [the views along i and j, respectively, with a common k axis—see Fig. 1(b)], the intensities in the side view $I_{ik}^{(2)}$ impose a weighting on the voxels along i, which are summed in the projection shown in $I_{jk}^{(2)}$. We can think of the structure as being rotated within the fixed i, j, k grid, and as examining two perpendicular projections, along i and j [Fig. 1(b)]. The value of N used in Eq. (1), is the unweighted number of pixels along i. Using information from the perpendicular view, $I_{ik}^{(2)}$, we replace N in Eq. (1) with

$$N_{k\langle i\rangle} = \sum_{i=1}^{N} I_{ik}^{(2)} / \max_i I_{ik}^{(2)}, \qquad (2)$$

where $\max_i I_{ik}^{(2)}$ is the maximum value of $I_{ik}^{(2)}$ for a fixed k. This normalization ensures that $N_{k\langle i\rangle} \leq N$ and that no pixel is assigned a combinatoric weight greater than unity. If a pixel in $I_{ik}^{(2)}$ has low intensity, the ambiguity in the intensity distribution along projection $I_{jk}^{(2)}$ is reduced. The corresponding decrease in entropy contribution is effected here by decreasing N. Although improved estimates of $N_{k\langle i\rangle}$ might be obtained by pursuing the methods of Refs. [18–23], the heuristic presented here has the advantage of simplicity and is more than sufficient to illustrate our key point about the entropy lowering of the zone-axis views. The additional information from the $I_{ik}^{(2)}$ side view reduces the entropy inferred from the $I_{jk}^{(2)}$ projection alone. Thus, Eq. (1) with $N_{k\langle i\rangle}$ replacing N represents $S(I_{jk}^{(2)}|I_{ik}^{(2)})$—the entropy of the $I_{jk}^{(2)}$ projection given the information in the perpendicular $I_{ik}^{(2)}$ view. Although this solution for the perpendicular-projection problem is approximate [24], it does exhibit reasonable behavior.

The plots in the right half of Fig. 1(a) show the constrained entropy $S(I_{jk}^{(2)}|I_{ik}^{(2)})$ for the three models (two crystal orientations and one amorphous). The constrained entropy for the amorphous model (the solid line) is reduced and remains approximately constant with angle. The constrained entropies of the crystalline models (the dashed lines) are also reduced, but they are generally higher than the amorphous entropy, except where perpendicular crystal zone axes are encountered, where the constrained entropy falls pronouncedly. The high-entropy situation arises in crystals because, if a column is tilted such that it barely overlaps a neighboring column, this local worst-case scenario is periodically repeated and the whole image becomes relatively uninformative. These entropic characteristics confirm that, for crystals, the zone-axis views are the most valuable views for tomographic reconstruction, a fact already exploited by certain groups [6,8]. This result suggests that tomography of crystalline materials is inherently easier than tomography of amorphous materials.

To examine this hypothesis, tomographic reconstructions were performed using the crystal and amorphous models. Here, we test the significance of low- and high-entropy projections, though the entropy is not directly used in the numerical implementation for tomographic reconstruction, as it arises from the intrinsic order of the object. First, reconstructions at different spatial resolutions were carried out with projection data evenly spaced throughout 180° to examine systematic, qualitative differences between crystalline and amorphous solids expected from the entropic analysis. Then, a set of reconstructions was carried out with selectively removed projections to establish the role of low-entropy projections in tomography. Although it is not the paradigm generally used in tomography, reconstruction strategies are inherently entropy-reduction procedures. For atomic-resolution tomography, the solution to the reconstruction problem is sought in the form of a "gas" of atoms, of unknown type, number, and location within the volume. Each image projection acts to constrain the available volume per atom, with the associated configurational entropy decreasing as $\ln(V/N)$ until an unambiguously frozen distribution of atoms is reached—that is, V/N is minimized.

To test our findings with more realistic input images, we simulated scanning transmission electron microscope annular dark-field images for the three models, emulating the conditions used in a previous experimental study [4]. To reduce pixelation noise, projections were first computed as (1120×1120)-pixel arrays, then binned to 140×140 pixels. Sixty projections in three-degree steps, with a sampling of 0.0405 nm per pixel (after binning), were calculated as diffraction-limited views of the projected potential. Resolutions ranging between 0.16 and 0.26 nm were simulated, and to match published experiments, the total signal in the (140×140)-pixel images was held at 860 000 counts (entire image), including shot noise [4]. The resolution was adjusted by changing the reciprocal-space diameter of a circular aperture [24]. These parameters approximate typical experimental conditions but ignore dynamical scattering and decoherence effects arising from motions in the structure [30].

Tomographic reconstructions were carried out using a compressed sensing approach [31], employing a three-dimensional total-variation minimization methodology and incorporating a non-negativity constraint [24]. After tomographic reconstruction, atoms were first identified by cross-correlation with a three-dimensional Gaussian of comparable

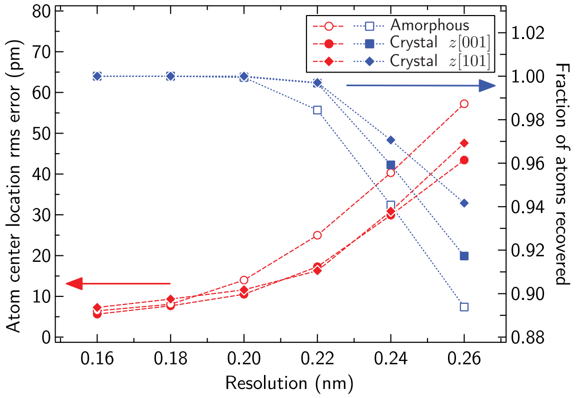

FIG. 2. Reconstruction quality of simulated crystalline and amorphous nanoparticles as a function of image resolution. (Left axis) Root-mean-square error of reconstructed atomic coordinates. (Right axis) The fraction of atoms recovered. Solid markers are for crystal reconstructions, open markers for the amorphous reconstruction.

dimensions to the reconstructed atoms, followed by subsequent refinement by fitting three-dimensional Gaussian functions at each identified atom position [24].

In both amorphous and crystalline samples, all 3409 atoms were recovered (having interatomic spacings of 0.235 nm) up to microscope resolutions of 0.2 nm, with the fraction of atoms recovered falling as the resolution deteriorated (Fig. 2, right axis). Atom centers were identified to within 10 pm (rms) of the known atom locations (Fig. 2, left axis). At resolution values greater than 0.2 nm, the crystalline reconstructions were significantly superior to the amorphous reconstructions, recovering a greater fraction of atoms with lower error. By these metrics, crystalline reconstructions are qualitatively different from amorphous reconstructions. Notably, the ideal samples considered here are free of image and tilt-axis misalignments, and of beam damage, experimental artifacts that will lower experimental reconstruction quality further. Zhu *et al.* [13] examined a model amorphous silicate particle and also concluded that tomography was possible. In practice, silicates are vulnerable to electron beam damage, and such specimen motions may ultimately be the limiting factor for tomographic reconstruction of amorphous materials. Broadly, and ignoring such displacement decoherence effects [30], for a given targeted recovery quality, crystalline reconstructions are systematically of higher quality, consistent with expectations from Fig. 1(a). Although the results are not presented here, the above conclusions hold for reconstructions of a crystal containing an oblique stacking fault. Moreover, isolated point defects do not substantially alter the entropic characteristics of the projection data, enabling the distinction of a vacancy in a crystalline particle from as few as eight projections [24]. Entropic analyses and tomographic reconstructions with larger particles (>45 000 and >100 000 atoms) showed similar behavior [24].

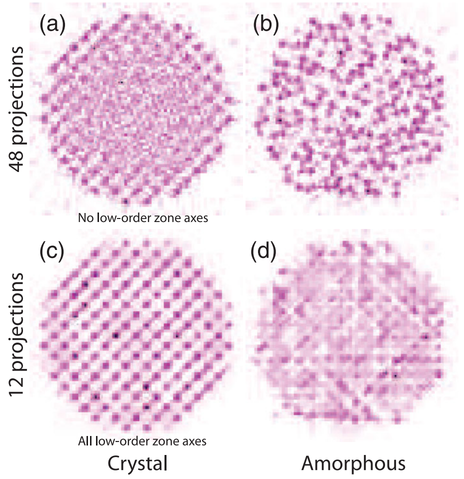

FIG. 3. Two-dimensional x-y planes ("orthoslices") from the centers of the reconstruction volumes for (a) crystalline and (b) amorphous samples using 48 "non-zone-axis" projections (only projections at angles corresponding to high-entropy crystalline projections). (c),(d) Orthoslices from the centers of the reconstruction volumes for (c) crystalline and (d) amorphous samples using only 12 "zone-axis" projections (only angles corresponding to low-entropy crystalline projections).

In order to specifically probe the relationship between reconstruction quality and the low-entropy projections used as input data, additional reconstructions were carried out where projections at tilt angles corresponding to (I) low-entropy projections or (II) high-entropy projections in the crystalline sample were selectively removed from both crystalline and amorphous samples [24]. Here, a single rotation axis ($z[001]$) was selected, exhibiting typical crystalline characteristics in the entropic analysis (Fig. 1). Figure 3 shows orthoslices (two-dimensional planes extracted from the three-dimensional reconstruction volume) for four input data sets (crystalline and amorphous for each of two cases). When 12 low-entropy projections were removed from the tilt-series input data, the crystalline sample failed to recover atoms located in the center of the particle, comprising in total ∼40% unrecovered atoms [Fig. 3(a)]. By contrast, the amorphous sample allowed for full recovery of all atoms with 48 of the original 60 projections as input data [Fig. 3(b)]. In the second case, using only 12 low-entropy projections, the crystalline sample enabled recovery of 3406 atoms (99.9%), with errors in atom positions comparable to the reconstruction using the full 60-projection tilt series [11 pm; see Fig. 3(c)]. However, ∼40% fewer total atoms were identified in the amorphous sample with significant errors in atom positions (72 pm), and the recovered atoms included "false positive" atom identifications [Fig. 3(d)]. Analogous tests with available experimental data showed similar behavior [32]. Taken together, these results reveal the critical role that low-entropy, low-order zone-axis projections play in tomographic reconstruction with accurate atom identification and precise atom location. For amorphous samples, a much larger number of input projections is required for comparable reconstruction quality. In practice, disruption of amorphous materials by the electron beam may prove to be a limitation [30], as it is for biological materials. Our results indicate that tomographic reconstruction of amorphous materials will not be as easy as that for crystals.

The structure in a sample inevitably determines the sensing-sampling relationship in tomography. This concept has seen highly successful application in compressed sensing methods where particular relationships between a sensing scheme (e.g., projection imaging) and a sampling protocol (e.g., the number or spacing of tilt angles) enables recovery from highly undersampled measurements [31]. However, the principle is more general and is applicable regardless of the particular reconstruction algorithm, whether or not it makes use of compressed sensing. The structure of such signals has also been noted in work on x-ray diffraction where the isolated distribution of signals in Bragg peaks for crystalline samples or the continuous distribution of signals in amorphous samples plays an important role [33]. Here, we have shown that in tomography at atomic resolution, the order of crystalline samples gives rise to inherent structure in the recorded real-space projection data, a significant departure from the amorphous case. Consequently, these problems are distinct recovery problems, best solved using methods suited to the particular characteristics of the recorded signals. Crucially, the informational entropy provides a description of the *input* data characteristics for understanding the role of individual projections in determining the reconstruction quality for atomic-resolution electron tomography. We note that low-entropy views become more common as crystallite size decreases.

Deviations from the simple crystalline and amorphous systems considered here, in the form of crystal defects and multielement compositions, will benefit from extensions of the proposed entropic analysis as a means of examining projection data. By examining a tilt-series data set, entropic analysis provides a way of determining the important projections for the reconstruction, facilitating emphasis during data acquisition for high signal and reduced noise at these sample orientations. These findings, moreover, are applicable to other length scales because the entropy is determined by structure in a sample, and atomic ordering is just one length scale where such structure may have an effect on tomographic reconstructions. Entropic analysis will also inform layered or zeolitic structures, particle aggregates, metamaterials, and other ordered samples examined by electron and x-ray tomography.

M. M. J. T is grateful for the support from the Leverhulme Trust and from the U.S. Department of Energy, Contract No. DE-AC02-06CH11357. R. K. L. acknowledges support from a Clare College Junior Research Fellowship. S. M. C. and P. A. M. acknowledge funding from the European Research Council under the European Union's Seventh Framework Program (FP7/2007–2013)/ERC Grant Agreement No. 291522-3DIMAGE. C.-B. S. acknowledges support from the Leverhulme Trust project "Breaking the non-convexity barrier," EPSRC Grant No. EP/M00483X/1, EPSRC Centre Grant No. EP/N014588/1, and CHiPS (the Horizon 2020 RISE project grant). R. T. acknowledges funding from EPSRC Grant No. EP/L016516/1 for the Cambridge Centre for Analysis. R. T. and C.-B. S. also acknowledge the Cantab Capital Institute for the Mathematics of Information. M. B. acknowledges the Isaac Newton Trust and the Leverhulme Trust Early Career Fellowship "Learning from mistakes: A supervised feedback-loop for imaging applications."

---

[*] treacy@asu.edu

[1] C.-C. Chen, C. Zhu, E. R. White, C.-Y. Chiu, M. C. Scott, B. C. Regan, L. D. Marks, Y. Huang, and J. Miao, Nature (London) **496**, 74 (2013).
[2] P. Rez and M. M. J. Treacy, Nature (London) **503**, E1 (2013).
[3] J. Miao, C.-C. Chen, C. Zhu, M. C. Scott, E. R. White, C.-Y. Chiu, B. C. Regan, Y. Huang, and L. D. Marks, Nature (London) **503**, E1 (2013).
[4] R. Xu, C.-C. Chen, L. Wu, M. C. Scott, W. Theis, C. Ophus, M. Bartels, Y. Yang, H. Ramezani-Dakhel, M. R. Sawaya *et al.*, Nat. Mater. **14**, 1099 (2015).
[5] J. Miao, P. Ercius, and S. J. L. Billinge, Science **353**, aaf2157 (2016).
[6] B. Goris, A. De Backer, S. Van Aert, S. Gómez-Graña, L. M. Liz-Marzán, G. Van Tendeloo, and S. Bals, Nano Lett. **13**, 4236 (2013).
[7] M. Azubel, J. Koivisto, S. Malola, D. Bushnell, G. L. Hura, A. L. Koh, H. Tsunoyama, T. Tsukuda, M. Pettersson, H. Häkkinen *et al.*, Science **345**, 909 (2014).
[8] B. Goris, J. De Beenhouwer, A. De Backer, D. Zanaga, K. J. Batenburg, A. Sánchez-Iglesias, L. M. Liz-Marzán, S. Van Aert, S. Bals, J. Sijbers *et al.*, Nano Lett. **15**, 6996 (2015).
[9] Y. Yang, C.-C. Chen, M. C. Scott, C. Ophus, R. Xu, A. Pryor, L. Wu, F. Sun, W. Theis, J. Zhou *et al.*, Nature (London) **542**, 75 (2017).
[10] D. N. Mastronarde, J. Struct. Biol. **120**, 343 (1997).
[11] X.-C. Bai, G. McMullan, and S. H. W. Scheres, Trends Biochem. Sci. **40**, 49 (2015).
[12] T. A. M. Bharat and S. H. W. Scheres, Nat. Protoc. **11**, 2054 (2016).
[13] C. Zhu, C.-C. Chen, J. Du, M. R. Sawaya, M. C. Scott, P. Ercius, J. Ciston, and J. Miao, Phys. Rev. B **88**, 100201 (2013).
[14] M. M. J. Treacy, J. M. Gibson, L. Fan, D. J. Paterson, and I. McNulty, Rep. Prog. Phys. **68**, 2899 (2005).
[15] P. M. Voyles and J. Hwang, *Fluctuation Electron Microscopy* (John Wiley & Sons, New York, 2012).
[16] G. T. Barkema and N. Mousseau, Phys. Rev. B **62**, 4985 (2000).
[17] W. Feller, *An Introduction to Probability Theory and Its Applications*, Vol. 1, 3rd ed. (John Wiley & Sons, New York, 1968).
[18] H. J. Ryser, Can. J. Math. **9**, 371 (1957).
[19] R. A. Brualdi, Linear Algebra Appl. **33**, 159 (1980).
[20] R. A. Brualdi and T. Michael, Linear Algebra Appl. **114**, 181 (1989).
[21] W. Y. Chen, J. Comb. Theory Ser. A **61**, 153 (1992).

[22] T. Werner, in *Proceedings of the Ninth International Conference on Computer Vision* (IEEE Computer Society Press, Washington, DC, 2003), Vol. 2, p. 1011.

[23] A. Barvinok, Linear Algebra Appl. **436**, 820 (2012).

[24] See Supplemental Material at http://link.aps.org/supplemental/10.1103/PhysRevLett.119.166101, which includes Refs. [25–29], for further details on entropic analysis, implementation of the tomographic reconstruction and processing methods, and reconstructions with selected projections removed, and for additional visualizations of tomographic reconstructions.

[25] L. I. Rudin, S. Osher, and E. Fatemi, Physica D (Amsterdam) **60D**, 259 (1992).

[26] D. Donoho, IEEE Trans. Inf. Theory **52**, 1289 (2006).

[27] A. Chambolle and T. Pock, J. Math. Imaging Vision **40**, 120 (2011).

[28] W. van Aarle, W. J. Palenstijn, J. De Beenhouwer, T. Altantzis, S. Bals, K. J. Batenburg, and J. Sijbers, Ultramicroscopy **157**, 35 (2015).

[29] M. Benning, computer code Object-Oriented MATLAB-Framework for Inverse Problems (OOMFIP), version 0.5, 2016, https://doi.org/10.17863/CAM.281.

[30] A. Rezikyan, Z. J. Jibben, B. A. Rock, G. Zhao, F. A. M. Koeck, R. F. Nemanich, and M. M. J. Treacy, Microsc. Microanal. **21**, 1455 (2015).

[31] R. K. Leary, Z. Saghi, P. A. Midgley, and D. J. Holland, Ultramicroscopy **131**, 70 (2013).

[32] B. D. A. Levin, E. Padgett, C.-C. Chen, M. C. Scott, R. Xu, W. Theis, Y. Jiang, C. Ophus, H. Zhang *et al.*, Sci. Data **3**, 160041 (2016).

[33] J. Miao, P. Charalambous, J. Kirz, and D. Sayre, Nature (London) **400**, 342 (1999).